

One-dimensional asymmetrically interacting quantum droplets in Bose-Bose mixtures

Huiyun Xiao,^{1,*} Xinran Zhang,^{1,*} Junli Liu,¹ Xucong Du,³ Xiao-Long Chen,^{1,2,†} and Yunbo Zhang^{1,‡}

¹*Department of Physics and Zhejiang Key Laboratory of Quantum State Control and Optical Field Manipulation, Zhejiang Sci-Tech University, Hangzhou 310018, China*

²*Lanzhou Center for Theoretical Physics, Key Laboratory of Theoretical Physics of Gansu Province, Key Laboratory of Quantum Theory and Applications of MoE, Gansu Provincial Research Center for Basic Disciplines of Quantum Physics, Lanzhou University, Lanzhou 730000, China*

³*School of Physics, Zhengzhou University, Zhengzhou 450001, China*

(Dated: January 26, 2026)

We theoretically investigate ground-state properties and collective excitations of one-dimensional quantum droplets in asymmetric Bose-Bose mixtures with unequal intraspin interactions. Using the extended Gross-Pitaevskii equation supported by variational and sum-rule methods, we show that the intraspin interaction ratio substantially alters the droplet's density profile, driving a transition from Gaussian-like to flat-top shapes. By examining two experimentally relevant parameter regions, we analyze density profiles, radii, peak densities, and excitation spectra to distinguish quantum phases and to depict phase diagrams in the space of asymmetric interaction ratio and total atom number. We carefully study the frequencies of both well-known dipole and breathing modes and less-explored spin dipole and spin breathing modes. The breathing mode frequency decreases monotonically with interaction ratio, approaching asymptotically the result of a conventional weakly interacting Bose gas. It varies non-monotonically with total atom number, peaking at a critical point that highlights the crucial role of quantum fluctuations. In contrast, spin modes display distinct temporal spin density distributions and reveal in-phase and out-of-phase relative dynamics between components. Their frequencies depend instead monotonically on the interaction ratio and atom number. Our results provide a comprehensive understanding of asymmetric quantum droplets and link to experimentally accessible regimes in ultracold ^{39}K atomic gases.

I. INTRODUCTION

Quantum droplets represent an emergent quantum state within ultracold atomic gases. Their existence challenges the conventional understanding that attractive Bose-Einstein condensates (BECs) require external trapping potentials for stability. These self-bound quantum droplets, sustained by a delicate balance between mean-field (MF) two-body interactions and quantum-fluctuation-induced Lee-Huang-Yang (LHY) correction (or three-body interactions), can form spontaneously without external confinement and exhibit distinctive macroscopic quantum properties and nonlinear dynamical behaviors [1–5]. After the innovative proposal of the stabilization mechanism, this novel dilute quantum-droplet state has been successfully observed in Bose-Bose mixtures with isotropic contact interactions [6–13], and in BECs with anisotropic dipolar interactions [14–19]. Similar stabilization mechanisms have been further identified in Bose-Fermi mixtures [20, 21] and dipolar mixtures [22, 23]. Nowadays, the intriguing intrinsic properties render quantum droplets an ideal platform for investigating self-organization phenomena and non-equilibrium dynamics in many-body quantum systems. Meanwhile, the successful developments in these experiments of quantum droplets have also stimulated intensive

and extensive investigations into this novel quantum state [24–27].

A. Bulgac proposed that three-body Efimov correlations can compromise the attractive mean-field two-body interactions to support the existence of self-bound dilute Bose and Fermi quantum droplets [2]. However, this scheme is very tough to achieve due to the severe three-body loss in the atomic experiments. Later in 2015, D.S. Petrov conducted groundbreaking research on two-component Bose gases within the framework beyond mean-field theory [3]. The crucial role of the higher-order LHY energy correction term induced by quantum fluctuation effects is revealed to stabilize the system against collapse and leads to the formation of a self-bound state. This stabilization mechanism is subsequently extended to low-dimensional systems [4], establishing a universal theoretical system for describing the ground state and dynamic properties of quantum droplets. These pioneering works stimulated fruitful experiments of quantum droplets in Bose-Bose mixtures to study liquid-to-gas transition [6, 7, 9], soliton-to-droplet transition [8], multiple quantum droplets [13], expansion dynamics [7, 12], collisions [10], and monopole oscillations [11]. Meanwhile, a series of theoretical methods, including quantum Monte Carlo methods [28, 29], non-perturbative variational Euler-Lagrange method [30], bosonic pairing theory [31], higher-order Beliaev's approach [32], Gaussian state theory [33], and thermodynamic approach [34], have been developed to complementarily explore the properties of this novel self-bound state in binary Bose mixtures. These theoretical approaches stimulated extensive and intensive investigations of quantum droplets

* These authors contributed equally to this work

† xiaolongchen@zstu.edu.cn

‡ ybzhang@zstu.edu.cn

in bosonic mixtures, such as studies of soliton-droplet transition [35] or liquid-gas coexistence [36], novel vortex quantum droplets [37–40], effect of thermal fluctuations [41], dimensional crossover [42], collisional or rotational properties [43–47], and low-energy spectrum or collective excitations [48–55], etc. However, most existing studies adopt symmetric intraspin interactions (i.e., $g_1 = g_2$ with balanced atomic mixtures) to describe the quantum-droplet state using a scalar wave function, leaving the role of interaction asymmetry largely unexplored [56–58], which is closely associated to the current experiments of quantum droplets in Bose mixtures [6–13]. Furthermore, these works focus primarily on conventional total-density-dependent collective modes, with minimal attention given to less-studied spin-dependent collective modes [59–61].

In this work, we investigate the ground-state properties and collective excitation modes of one-dimensional quantum droplets in weakly interacting binary Bose gases with asymmetric intraspin interactions, by employing both numerical and analytical approaches as described in our previous works [45, 54, 55]. The ground-state wave function is obtained by numerically solving the static extended Gross–Pitaevskii equation (GPE) for quantum droplets. In terms of this ground-state wave function, we systematically examine the density profile, cloud size, and peak density of the quantum droplets under varying interaction-strength ratio, trapping strength, and total atom number. The numerical results are compared with those obtained from a variational approach with a super-Gaussian Ansatz for the droplet wave function. Furthermore, we introduce controlled perturbations to excite collective excitations in trapped droplets, and adopt the time-dependent extended GPE to describe the behaviors of specific collective modes, such as the well-studied dipole, monopole (breathing), as well as the less-studied spin-dipole and spin-monopole (spin-breathing) modes. Additionally, based on the super-Gaussian variational ansatz, we derive analytical expressions for the dipole-mode and breathing-mode frequencies within a sum-rule formalism to verify the numerical predictions.

The remainder of this paper is organized as follows. Sec. II begins with the energy functional for quantum droplets in a one-dimensional weakly interacting two-component Bose mixture. We then derive the extended Gross–Pitaevskii equations with an external harmonic trapping potential to describe this quantum droplet. Meanwhile, a variational approximation with a super-Gaussian Ansatz for the droplet wave function and the sum-rule approach are introduced. In Sec. III, we apply these methods to consider the roles of interaction-strength ratio, trapping strength, and total atom number on droplets, and compute the ground-state properties as well as the low-lying collective modes under asymmetric intraspin interactions. The influence of the interaction-strength ratio, trapping strength, and total atom number on the quantum droplets is systematically discussed. Finally, Sec. IV provides concluding remarks and an out-

look for future work.

II. THEORETICAL FRAMEWORK

In this section, we present two theoretical methods for investigating the ground-state properties and collective excitations of one-dimensional quantum droplets in weakly interacting Bose–Bose mixtures, both qualitatively and quantitatively. We numerically solve the extended GPE to provide a comprehensive study of the static and dynamic behaviors, which will be compared with predictions from a variational approach (VA) and a sum-rule approach.

A. Time-dependent extended Gross–Pitaevskii equation

We consider the quantum droplet in a one-dimensional (1D) weakly interacting Bose–Bose mixture with equal masses (i.e., $m = m_1 = m_2$) stabilized by the beyond MF or LHY energies arising from quantum fluctuations [3]. This quantum droplet can be described by the effective energy functional including the LHY energy corrections [4]

$$E^{(1D)} = \frac{(n_1\sqrt{g_1} - n_2\sqrt{g_2})^2}{2} + \frac{g\delta g(n_1\sqrt{g_1} + n_2\sqrt{g_2})^2}{(g_1 + g_2)^2} - \frac{2\sqrt{m}(n_1g_1 + n_2g_2)^{3/2}}{3\pi\hbar}, \quad (1)$$

near the collapsing point $0 < \delta g \equiv g + g_{12} \ll g \equiv \sqrt{g_1g_2}$ of the mean-field level. Here, the first two terms at the right side of Eq. (1) correspond to mean-field energy, and the third term is the LHY energy. $g_{1,2}$ and g_{12} are the effective 1D intra- and interspin interaction strengths, which are repulsive and attractive in this quantum droplet regime, respectively, i.e., $g_{1,2} > 0$ and $g_{12} < 0$. $n_{1,2}$ represents the density of two spin components.

In this work, instead of considering the symmetric interaction (i.e., $g_1 = g_2$) as in most previous works, we emphasize the effect of asymmetric intraspin interactions with $g_1 \neq g_2$ on quantum droplets and introduce a dimensionless interaction ratio

$$\lambda \equiv \frac{g_1}{g_2}, \quad (2)$$

to quantify this asymmetry. For this purpose, by starting from the energy functional in Eq. (1) and employing the Heisenberg equation of motion, we derive the extended GPE for an asymmetric 1D Bose–Bose mixture in an external harmonic trap [4, 62], being

$$i\hbar \frac{\partial}{\partial t} \psi_\sigma = \left[H_{\text{ho}} + \left(g_\sigma + \frac{2gg_\sigma\delta g}{(g_1 + g_2)^2} \right) n_\sigma - \left(g - \frac{2g^2\delta g}{(g_1 + g_2)^2} \right) n_{\bar{\sigma}} - \frac{\sqrt{m}}{\pi\hbar} g_\sigma (g_1 n_1 + g_2 n_2)^{\frac{1}{2}} \right] \psi, \quad (3)$$

for spin component $\sigma = \{1, 2\}$ with different spin indices $\sigma \neq \bar{\sigma}$. $H_{\text{ho}} = -\frac{\hbar^2}{2m}\partial_x^2 + V_{\text{ext}}(x)$ denotes the single-particle Hamiltonian of a harmonic oscillator, and the frequency $\omega_x = \kappa\omega_0$ of the trapping potential $V_{\text{ext}}(x) = \frac{1}{2}m\omega_x^2x^2$ can be tuned by a parameter κ . $n_\sigma \equiv |\psi_\sigma|^2$ represents the local density of two spin components, and the wave functions are normalized to N , i.e., $\sum_{\sigma=1,2} \int |\psi_\sigma|^2 dx = N$. In practical calculations, we adopt a set of characteristic units related to the harmonic oscillator, i.e., the characteristic energy $E_0 \equiv \hbar\omega_0$ and length $x_0 = \sqrt{\hbar/(m\omega_0)}$, to obtain dimensionless extended GPE. By separating the variables via $\psi_\sigma(x, t) = \psi_\sigma(x)e^{-i\mu t}$ with the chemical potential μ and numerically solving the time-independent coupled equations, we can study the static properties of quantum droplets.

To further investigate the crucial low-energy collective excitations or elementary excitations of this quantum many-body system, we can slightly perturb the static system to excite it and probe its responses as in realistic cold atomic experiments. In general, we consider four typical low-energy collective excitations here, i.e., the familiar dipole and breathing (or monopole) modes, and the spin dipole and spin breathing modes [59–61, 63], by developing distinct modulations of the external trapping potential and studying the corresponding dynamical behaviors of the system via the time-dependent extended GPE in Eq. (3). In practice, we excite these four collective modes by abruptly changing the external potential $V_{\text{ext}}(x)$ to a slightly changed potential $V'_{\text{ext}}(x)$ as in our previous works [54, 55]. The specific form is given as

$$V'_{\text{ext}}(x) = \begin{cases} \frac{1}{2}m\omega_x^2(x - \mathcal{I}\delta x)^2, \\ \frac{1}{2}m(1 + \mathcal{I}\chi)^2\omega_x^2x^2, \\ \frac{1}{2}m\omega_x^2(x - \sigma_z\delta x)^2, \\ \frac{1}{2}m(1 + \sigma_z\chi)^2\omega_x^2x^2, \end{cases} \quad (4)$$

for four respective collective modes. Here, δx is a small displacement and $\chi \ll 1$ is a small factor to tune the trapping frequency. \mathcal{I} and σ_z denote the 2×2 identity and Pauli matrices, respectively.

For instance, by applying the same displacement $\mathcal{I}\delta x$ for both spin components as described by the first term in Eq. (4), the dipole mode is excited with the total density profile oscillating about the origin, which can be characterized by the time-dependent center-of-mass displacement $\langle x(t) \rangle$ averaged on the time-dependent wave function. Similarly, we tune the trapping frequency with the same factor $\mathcal{I}\chi$ for both spin components as the second term in Eq. (4) and excite the monopole or breathing mode oscillation. In this mode, the atomic cloud will expand and contract monopolarly, behaving as breathing, which can be characterized by the dynamical evolution of the cloud size or the squared size $\langle x^2(t) \rangle$. In contrast, we employ spin-dependent displacements $\sigma_z x$ or trapping frequency variation $\sigma_z \chi$ as in the last two terms in Eq. (4) to excite the spin dipole and spin breathing modes, respectively. These two spin-related excitations reveal the

relative motions of the two spin components, i.e., two spin densities counterpropagating along the x axis in the spin dipole mode, or exhibiting relative trends of expansion and contraction in the spin breathing mode. They can be further characterized by the corresponding displacement $\langle \sigma_z x(t) \rangle$ and the squared size $\langle \sigma_z x^2(t) \rangle$ of the spin density, respectively. Eventually, after slightly perturbing the system to excite respective collective modes, we calculate the time-dependent wave functions as well as the evolution of the corresponding physical observables $\langle \mathcal{O}(t) \rangle$ by numerically solving the time-dependent extended GPE in Eq. (3). The mode frequency is further extracted from the frequency peaks in the Fourier analysis of $\langle \mathcal{O}(t) \rangle$ and the spatiotemporal evolution of the density profile possessing characteristic oscillation patterns.

B. Variational approximation and the sum-rule approach

In addition to the extended GPE, we further introduce a variational approximation to provide a qualitative and quantitative description of the static properties of quantum droplets in this asymmetric intraspin-interaction configuration. Meanwhile, the sum-rule approach is adopted to derive an explicit analytic expression of the dipole and breathing mode frequencies of quantum droplets that are compared to the numerical results. As studied in previous works [4, 45, 48, 51, 52, 54], the quantum fluctuations stabilized droplets exhibit a unique flat-top structure in the density distribution at relatively large atom number in sharp contrast to the conventional Gaussian state. Therefore, one can usually employ the so-called super-Gaussian variational *Ansatz* to describe the spinor wave function of self-bound quantum droplets, being [49, 52, 54]

$$\psi_1^{SG}(x) = \sqrt{\frac{N\alpha}{\Gamma(\frac{1}{2\alpha})(\sqrt{\lambda} + 1)\sigma}} e^{-\frac{1}{2}(\frac{x}{\sigma})^{2\alpha}}, \quad (5a)$$

$$\psi_2^{SG}(x) = \sqrt{\frac{N\alpha\sqrt{\lambda}}{\Gamma(\frac{1}{2\alpha})(\sqrt{\lambda} + 1)\sigma}} e^{-\frac{1}{2}(\frac{x}{\sigma})^{2\alpha}}, \quad (5b)$$

with two variables, i.e., the cloud width σ and the exponent factor α [64]. Here, $\Gamma(x)$ is the Gamma function. The width determines the size of the droplet, while the exponent factor reveals the Gaussian or flat-top nature in the density profile. In practice, we substitute the variational ansatz Eq. (5) into the total energy functional including Eq. (1) as well as the kinetic and external trapping energies, and minimize the energy to obtain the extrema across the parameter spaces. The explicit equations of the extremum points, as well as their behaviors, can be seen in detail in Appendix A. With the calculated extrema, the wave function of quantum droplets can be constructed to study the static properties. Furthermore, the sum-rule approach is employed to provide

an approximate upper bound for the frequencies of relevant collective excitations [65–67]. One can introduce the energy-weighted moments and relate them to the commutation relations of specific operators. Thus, the frequencies of the collective excitation can be estimated by the moment ratios. For instance, by introducing the excitation operator of the dipole mode $\hat{F} = \sum_{i=1}^N \hat{x}_i$, the frequency of the dipole mode is bounded by the moment ratio m_3/m_1 with $m_1 = \frac{1}{2}\langle\psi|[\hat{F}^\dagger, [\hat{H}, \hat{F}]]|\psi\rangle$ and $m_3 = \frac{1}{2}\langle\psi|[[\hat{F}^\dagger, \hat{H}], [\hat{H}, [\hat{H}, \hat{F}]]]|\psi\rangle$ [66, 68]. In the framework of first quantization, the Hamiltonian of a weakly interacting Bose mixture with $m_1 = m_2 = m$ is given as $\hat{H} = \sum_{i,\sigma} \left[-\frac{\hbar^2 \nabla_{i,\sigma}^2}{2m} + V_\sigma(x_i) \right] + \frac{1}{2} \sum_{i,j,\sigma,\sigma'} U_{\sigma,\sigma'}(x_i - x_j)$ with $i, j = \{1, 2, \dots, N\}$ and $\sigma, \sigma' = \{1, 2\}$. $V(x) = \frac{1}{2}m\omega_x^2 x^2$ represents the external potential in which the particle is placed, and $U_{\sigma,\sigma'}(x_i - x_j)$ describes the contact pseudopotentials between any two particles. This leads to the expression

$$\omega_d^2 = \frac{m_3}{m_1 \hbar^2} = \omega_x^2, \quad (6)$$

which verifies the Kohn theorem that the oscillation frequency of the dipole mode equals the frequency of the trapping potential. In addition, the frequency of the breathing mode can be calculated by the moment ratio $\omega_b^2 = \frac{m_1}{m_{-1} \hbar^2}$ of the energy-weighted moment m_1 to the inverse-energy-weighted moment m_{-1} with the excitation operator $\hat{F} = \sum_{i=1}^N \hat{x}_i^2$. Here, one can instead use the relation between the inverse energy-weighted moment and the static polarization $m_{-1} = (1/2)\chi$ with $\chi = -\frac{2N}{m} \frac{\partial \langle x^2 \rangle}{\partial \omega_x^2}$ and obtains the useful result of the breathing mode frequency $\omega_b^2 = \frac{m_1}{m_{-1} \hbar^2} = -\sigma \frac{\partial \omega_x^2}{\partial \sigma}$ [51, 55, 67]. After some straightforward algebra, we derive an analytic expression for the breathing mode frequency ω_b in terms of the extremum points (α_0, σ_0) as

$$\begin{aligned} \omega_b^2 = & \frac{\hbar^2 \alpha_0^2 \Gamma(2 - \frac{1}{2\alpha_0})}{m^2 \sigma_0^4 \Gamma(\frac{3}{2\alpha_0})} + 3 \left(\frac{1}{2} \right)^{\frac{1}{2\alpha_0}} \frac{N \alpha_0 \sqrt{\lambda} (g_{12} + g_2 \sqrt{\lambda})}{m \sigma_0^3 \Gamma(\frac{3}{2\alpha_0}) (\sqrt{\lambda} + 1)^2} \\ & - \frac{5}{6} \left(\frac{2}{3} \right)^{\frac{1}{2\alpha_0}} \sqrt{\frac{N \alpha_0 \Gamma(\frac{1}{2\alpha_0})}{\sigma_0^5}} \frac{(g_2 \sqrt{\lambda})^{\frac{3}{2}}}{\sqrt{m \pi \hbar \Gamma(\frac{3}{2\alpha_0})}}. \end{aligned} \quad (7)$$

Therefore, after calculating the extremum points (α_0, σ_0) in the minimization, the corresponding frequencies of the collective excitations $\omega_{d,b}$ can be constructed to be compared with the results from the extended GPE.

III. RESULTS AND DISCUSSIONS

As in the experiments with cold atoms [69–71], we can carefully manipulate the confining frequencies of external harmonic traps to achieve the cigar-shaped system or 1D geometry adopted in this work. Hence, by flexibly tuning the confinement trapping frequencies

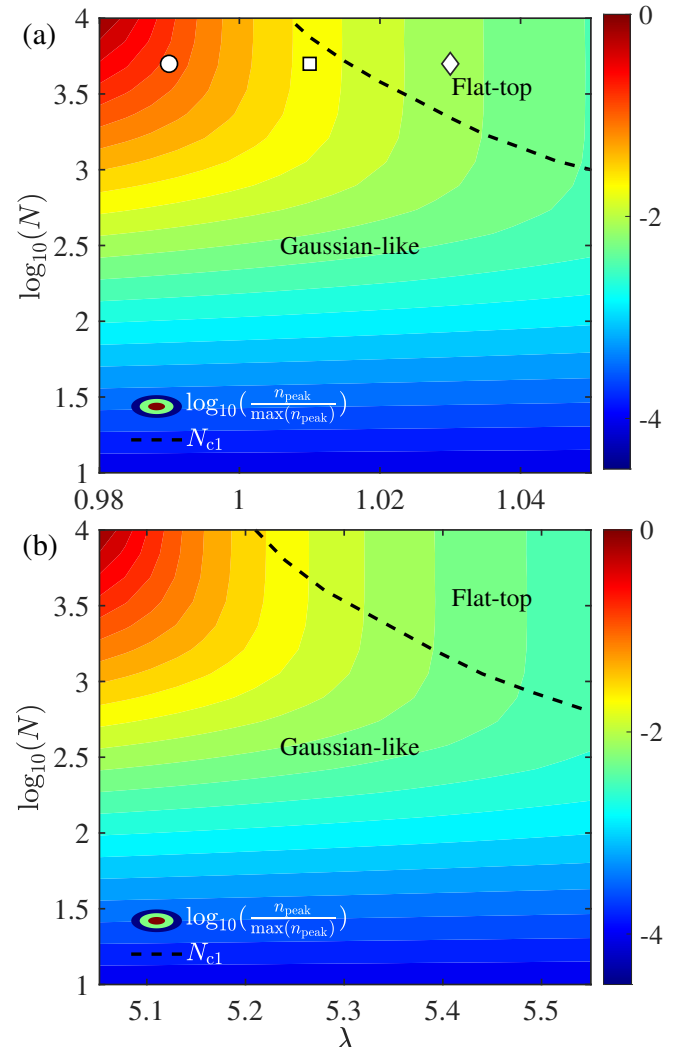


FIG. 1: Typical phase diagram in the parameter space of interaction strength ratio λ and total atom number N . Subplots (a) and (b) denote the contour plots of the peak density of quantum droplets in the λ - $\log_{10}(N)$ plane at the parameter regions I and II described in the main text, respectively. The gradient color represents the scaled peak density $\log_{10}[n_{\text{peak}} / \max(n_{\text{peak}})]$. The dashed line marks the critical position N_{c1} to distinguish the phase boundary between Gaussian-like and flat-top phases, corresponding to the saturation point of the peak density. Here, the hollow circle, square, and diamond in subplot (a) denote the positions of three typical density profiles in Fig. 3(a).

$(\omega_x, \omega_y = \omega_z = \omega_\perp)$, we can realize the quasi-1D geometry along the x axis with the effective 1D interaction strength $g^{(1D)} = \frac{4\hbar^2 a_s}{ml_\perp^2} (1 - \mathcal{C} \frac{a_s}{l_\perp})^{-1}$ [72], with $\mathcal{C} \approx 1.4603$, or $g^{(1D)} \approx \frac{\hbar^2 a_s}{2ml_\perp^2}$ [4], with the oscillator length l_\perp in the tightly confined y - z plane ($\omega_\perp \gg \omega_x$). By taking two groups of quasi-1D confinement closely related to the experiments, we obtain two sets of dimension-

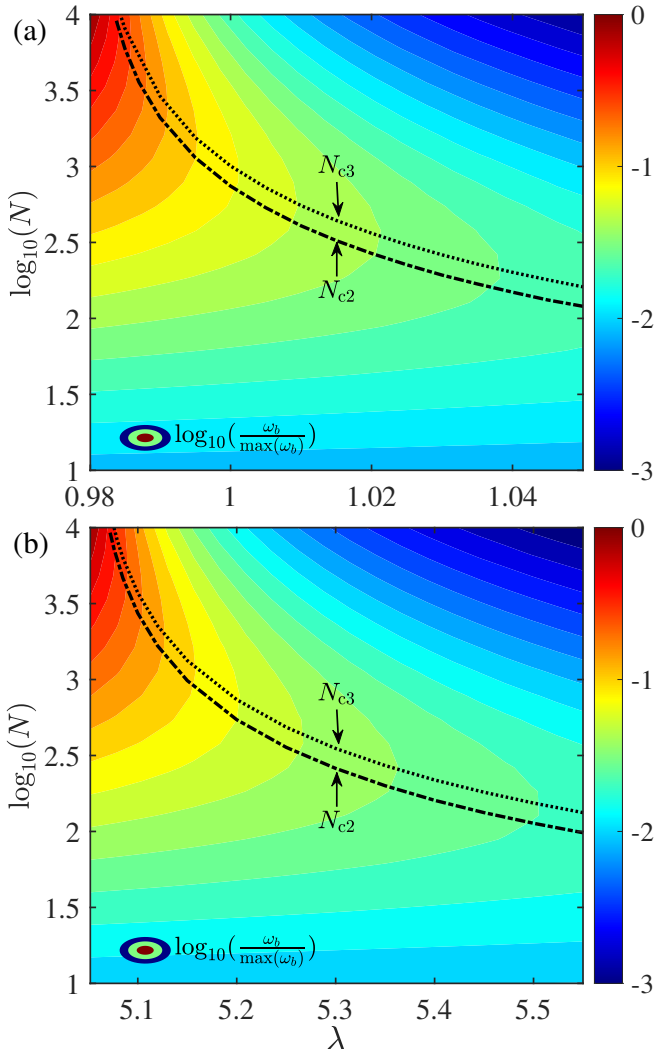


FIG. 2: Breathing mode frequency in the parameter space of interaction strength ratio λ and total atom number N . Subplots (a) and (b) denote the contour plots of the breathing mode frequency of quantum droplets in the λ - $\log_{10}(N)$ plane at the parameter regions I and II, respectively. The gradient color represents the scaled peak density $\log_{10}[n_{\text{peak}}/\max(n_{\text{peak}})]$. Here, the dash-dotted and dotted lines, i.e., N_{c2} and N_{c3} , mark the minimum of the root-mean-square radius and the maximum of the breathing mode frequency, respectively.

less effective 1D interaction strengths $g_2 = 0.100, g_{12} = -0.099, g_1 \in [0.098, 0.105]$ and $g_2 = 0.089, g_{12} = -0.200, g_1 \in [0.449, 0.494]$, giving rise to two groups of the interaction ratio with $\delta g/g \ll 1$, i.e., region I with $\lambda \in [0.98, 1.05]$ near unity and region II with $\lambda \in [5.05, 5.55]$ away from unity. To further consider a binary bosonic gas with tunable interactions, we can utilize the Feshbach resonance of ^{39}K atoms at $B_0 = 58.92\text{G}$ where the intra- and interspecies s -wave scattering lengths a_{22} and a_{12} in three dimensions are approximately constant

while the intraspecies scattering length a_{11} spans over a wide range [73]. Taking a typical harmonic confinement $(\omega_x, \omega_{\perp}) = 2\pi \times [300, 1.85 \times 10^4]\text{Hz}$ from Ref. [71] for a binary ^{39}K gas, the calculated interaction ratio spans the range $[0.21, 7.09]$ with magnetic field B in $[50, 58]\text{G}$, which covers both parameter sets used in this work.

A. Phase diagram

In Fig. 1, we present the typical phase diagrams of the free-space (i.e., $\kappa = 0$) quantum droplets in the asymmetrically-interacting Bose-Bose mixture modulated by the interaction strength ratio $\lambda \equiv g_1/g_2$ and the total atom number N in two parameter regions (a) I and (b) II. The scaled peak density $\log_{10}[n_{\text{peak}}/\max(n_{\text{peak}})]$ in Fig. 1 is calculated to illustrate typical phases in gradient colors. Here, we have introduced a critical atom number N_{c1} to distinguish the phase boundary of the typical Gaussian-like and flat-top phases. N_{c1} is determined by the position where the peak density of the quantum droplet becomes saturated, which exhibits a monotonically decreasing behavior with respect to the ratio λ shown as the dashed line in Fig. 1. As N rises, the system manifests as a Gaussian-like quantum phase with a continuously increasing peak density and a varying cloud size. Above N_{c1} , the peak density remains unchanged, as shown by the vertically unchanged color above the dashed lines. This reveals the dominant contribution of the MF and LHY energies, and the system steps into a flat-top quantum droplet phase with a constant peak density.

In the same parameter regions I and II, we further calculate the breathing mode frequency and illustrate the contour plots of the scaled breathing mode frequency $\log_{10}[\omega_b/\max(\omega_b)]$ in Fig. 2. Two curves, namely N_{c2} and N_{c3} , are introduced and exhibit a monotonically decreasing behavior as the ratio λ rises. These two curves, represented by the dash-dotted and dotted lines, are relatively very close, corresponding to the minimum of the root-mean-square radius and the maximum of the breathing mode frequency, respectively. When N increases gradually towards these two curves, the role of the MF and LHY energies starts to become non-negligible and competes against the quantum pressure induced by the single-particle term. As a result, the system experiences a transition from a Gaussian-like phase to a flat-top phase. Near N_{c2} or N_{c3} , the effectively attractive MF and LHY energies compress the droplet against the repulsive quantum pressure to reach the minimum radius in the density profile. Meanwhile, the breathing mode frequency is pronouncedly enhanced and reaches a maximum, see Fig. 2 and details in the later section.

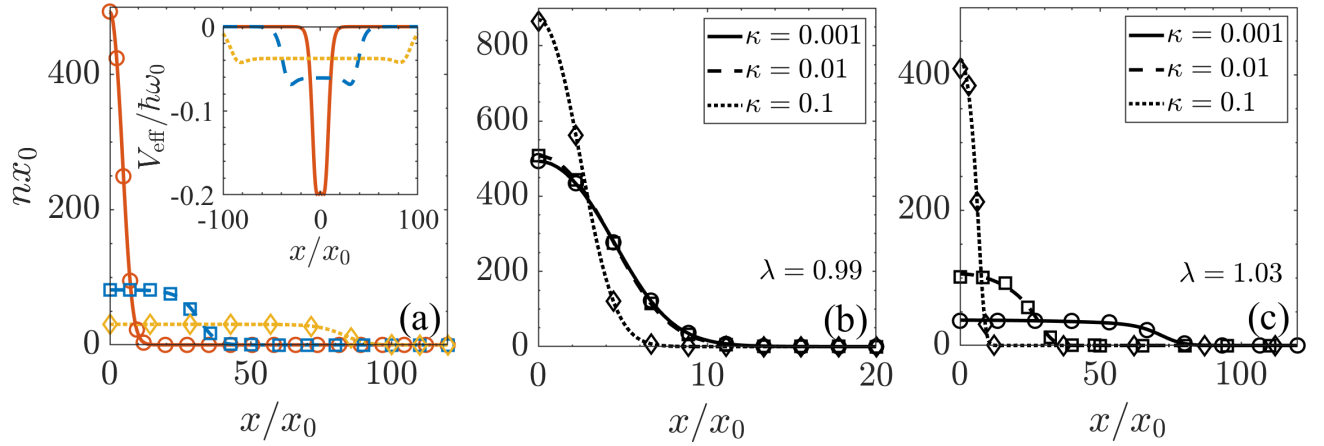


FIG. 3: Total density distribution n at various values of interaction ratio $\lambda = g_1/g_2$ and trapping potential strength κ . (a) density profiles without external potential (i.e., $\kappa = 0$) at three typical values of $\lambda = 0.99$ (red solid line), 1.01 (blue dashed line), 1.03 (yellow dotted line) in parameter region I. The corresponding results obtained from the variational approach are shown by the circles, squares, and diamonds. The inset shows the corresponding effective potentials owing to the mean-field and Lee-Huang-Yang energy contributions. (b, c) density profiles for $\lambda = 0.99$ and $\lambda = 1.03$ at three values of potential strength $\kappa = 0.001, 0.01$, and 0.1 , denoted by the solid, dashed, and dash-dotted curves, respectively.

B. Stationary properties

In Fig. 3, we present the ground-state density distributions at typical values of interaction ratio λ and trapping potential strength κ in parameter region I. In accordance with recent experiments on quantum droplets [6–10], we first focus on the parameter space near the symmetric point (i.e., $\lambda = 1$ or $g_1 = g_2$) with the total atom number $N = 5000$. In free space, as shown in Fig. 3(a), the effective potential V_{eff} in Eq. (3) contributed by the mean-field interaction and LHY correction changes from a harmonic-potential shape to a box-like shape as λ rises. As a consequence, the total density of the quantum droplet exhibits a Gaussian-like profile at $\lambda = 0.99$ (red solid curves), and turns into a flat-top structure at larger λ (blue dashed and yellow dotted curves). This gradual transition in the density of droplets from Gaussian-like to flat-top structure is reminiscent of the same condition as the total atom number increases in previous works [48, 51, 54, 55, 74], revealing the characteristic signature of a quantum phase transition in self-bound droplets. These three typical density profiles are located at different positions in the parameter space, as indicated by the hollow circle, square, and diamond in Fig. 1(a). In Fig. 3(b) and Fig. 3(c), the density profiles are present at three values of trapping potential strength $\kappa = 0.001, 0.01$, and 0.1 for $\lambda = 0.99$ and $\lambda = 1.03$, respectively. At small $\lambda = 0.99$, the Gaussian-like density profile is gradually compressed by the enhancing trapping potential as κ increases, maintaining the Gaussian structure with a much more localized shape and a higher peak density as shown in Fig. 3(b). In contrast, the flat-top density for $\lambda = 1.03$ in free space is significantly modified by

the increasing κ , transforming from a flat-top structure to a Gaussian-like distribution with the radius squeezed remarkably owing to the relatively strong trapping potential, see Fig. 3(c). Intriguingly, the analytical solutions denoted by the hollow symbols obtained from the super-Gaussian variational ansatz in Eq. (5) show excellent agreement with the numerical results denoted by the curves across all parameter regimes, as shown in Fig. 3.

To characterize the typical phases in quantum droplets, we turn to investigate the root-mean-square radius $\sqrt{\langle x^2 \rangle}$ and the peak density n_{peak} of two spin components as functions of the interaction ratio λ and total atom number N . In Fig. 4, the radius and peak density calculated by solving the extended GPE are presented as functions of λ in parameter region II at three values of trapping potential strength $\kappa = 0.001, 0.01$, and 0.1 as shown by the solid, dashed, and dotted curves, respectively. In general, the radii of two spin components [i.e., black curves in Fig. 4(a)] are the same while their peak densities [i.e., red and blue curves in Fig. 4(b)] are not, since the value of λ is far away from unity, giving rise to different atom numbers of two spin components. Near in free space, i.e., at sufficiently weak trapping potential with $\kappa = 0.001$, the radius in the black solid curve increases monotonically with λ as the system transitions from a Gaussian-like phase to a flat-top phase, consistent with the scenario illustrated in Fig. 3(a). As a result of a fixed total atom number, the two peak densities decrease gradually and tend to saturate at a specific value. This is because at relatively larger λ the system exhibits a flat-top structure in the density profile with a nearly constant peak density and an expanding radius as described in previous works [48, 50, 74]. At relatively stronger trapping potentials, i.e., $\kappa = 0.01$ and 0.1 shown

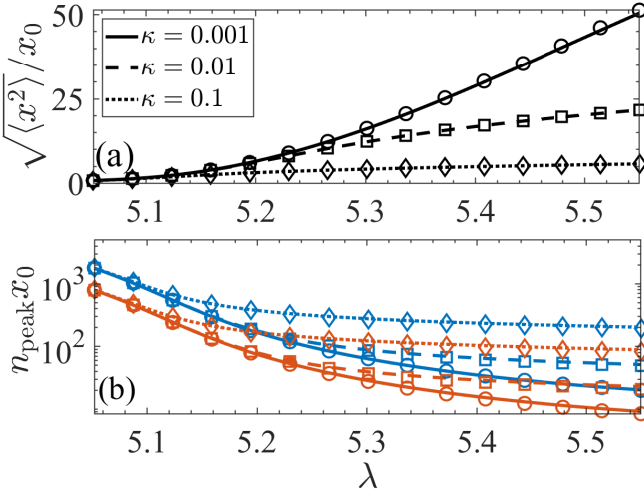


FIG. 4: (a) The root-mean-square radius $\sqrt{\langle x^2 \rangle}$ and (b) the peak density n_{peak} of two spin components at three values of trapping potential strength $\kappa = 0.001$ (solid lines), 0.01 (dashed lines), and 0.1 (dotted lines), as functions of the interaction ratio λ in parameter region II with $N = 5000$. The hollow circles, squares, and diamonds show the corresponding results obtained from the variational approach. The red and blue colors in (b) denote the results for spin components 1 and 2, respectively.

by dashed and dotted curves respectively, the variations in the radius and peak density become much more gentle and smooth. This can be understood as a consequence of the stronger confinement imposed by the external potential, which compresses the droplet into a smaller width and thus elevates its central density. The corresponding results obtained from the variational approach are denoted by the hollow symbols in Fig. 4, which show intriguingly a quantitative agreement with the numerical ones.

In Fig. 5, we further show the dependence of radius and the peak density of two spin components on total atom number N at different strengths of external trapping potential. Near in free space with $\kappa = 0.001$, the radius exhibits a non-monotonic behavior with respect to N , i.e., decreasing gradually to a minimum and then turning to increase significantly, as shown by the black solid line in Fig. 5(a). Meanwhile, the peak densities of both spin components increase monotonically and turn to saturate at the specific values as N rises, as shown by the red and blue solid lines in Fig. 5(b). These behaviors are reminiscent of our previous findings in Ref. [54]. At small N , the quantum pressure arising from the dominant kinetic energy pushes the atoms away to maintain a relatively large width. As N increases, a competing effectively attractive interaction owing to the MF and LHY energy terms will slightly squeeze the condensate, and hence the radius decreases relatively. We introduce the first critical value N_{c2} in Fig. 5(a), where the radius

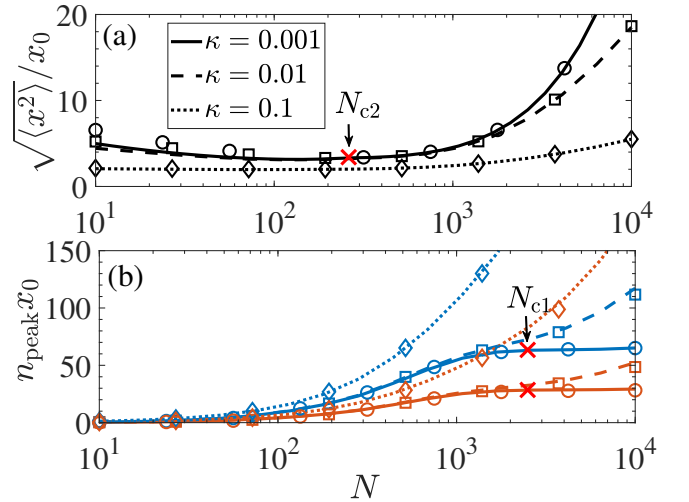


FIG. 5: (a) The root-mean-square radius $\sqrt{\langle x^2 \rangle}$ and (b) the peak density n_{peak} of two spin components at three values of trapping potential strength $\kappa = 0.001$ (solid lines), 0.01 (dashed lines), and 0.1 (dotted lines), as functions of the total atom number N with $\lambda = 5.3$. The hollow circles, squares, and diamonds show the corresponding results obtained from the variational approach. The red and blue colors in (b) denote the results for spin components 1 and 2, respectively. Here, the critical atom numbers N_{c1} and N_{c2} are determined by the saturated peak density of the quantum droplet, and the minimum of the radius, respectively.

reaches the minimum, see also the black dash-dotted lines in Fig. 1. At relatively large N , the system dominated by the LHY energy steps into the flat-top droplet phase characterized by a saturated peak density and an increasing width depending linearly on N . Similarly, the critical N_{c1} in Fig. 5(b) indicates the position where the peak density becomes constant, which is denoted by the black dashed lines in Fig. 1. At relatively stronger trapping potentials, i.e., $\kappa = 0.01$ and 0.1 shown by dashed and dotted curves respectively, the condensates are compressed significantly by the external confinement. As a result, the radius tends to be flat with the non-monotonic behavior disappearing, and the peak densities rise notably showing a linear dependence on N . Our results from the variational approach, presented in the hollow symbols in Fig. 5, show a good agreement with the numerical ones.

C. Collective excitation modes

Now we turn to the collective elementary excitations or collective modes of quantum droplets in this asymmetrically interacting 1D Bose-Bose mixture, which reveal the important dynamical properties of this novel phase and can be well probed in ultracold atomic experiments.

In Fig. 6, the frequencies of the dipole and breathing modes are shown as functions of the interaction ratio λ in

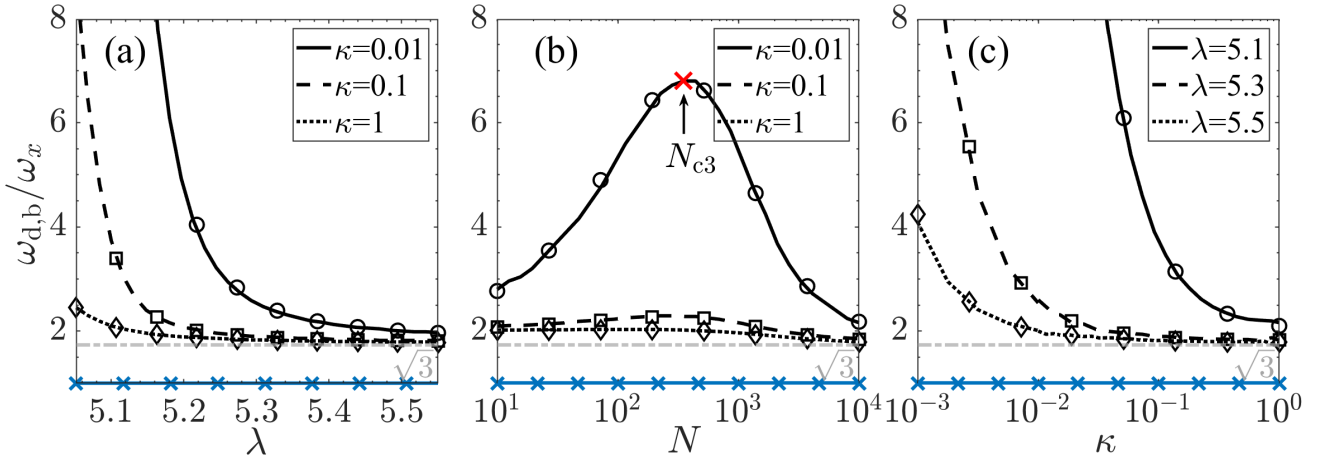


FIG. 6: The dipole mode (blue lines) and breathing mode (black lines) frequencies $\omega_{d,b}$, as functions of (a) interaction ratio λ with $N = 5000$, (b) total atom number N with $\lambda = 5.3$, and (c) trapping potential strength κ with $N = 5000$. The solid, dashed, and dotted lines in (a, b) represent three sets of trapping potential strength $\kappa = 0.01, 0.1, 1$, respectively, while they denote $\lambda = 5.1, 5.3, 5.5$ in (c). The hollow circles, squares, and diamonds show the corresponding results obtained from the variational approach. Here, the horizontal gray dashed line indicates the analytic breathing mode frequency $\omega_b = \sqrt{3}\omega_x$ for a conventional weakly interacting Bose gas. The critical atom number N_{c3} in the middle plot is determined by the maximum of the breathing mode frequency.

parameter region II, the total atom number N , and the trapping potential strength κ . Here, the curves indicate the numerical calculations via the EGPE, while the hollow symbols denote the corresponding results obtained from the sum-rule approach with a variational approximation. In Fig. 6(a), the breathing mode frequency ω_b in nearly free space (i.e., black solid lines) will significantly increase as λ decreases and tends to diverge at the left end. This is because at the left end of λ , the δg tends to be zero, thus the repulsive MF energy disappears and the attractive LHY energy leads the system to collapse. Moreover, larger trapping strengths κ , i.e., black dashed and dotted lines, lead to a more gradual decline in ω_b which asymptotically approaches the result of a weakly interacting 1D Bose gas $\omega_b = \sqrt{3}\omega_x$ [66, 67] (horizontal gray dash-dotted line) at the right side of λ . In Fig. 6(b), the breathing mode frequency of droplets in nearly free space (i.e., black solid lines) shows a pronounced non-monotonic behavior as the atom number N rises, i.e., significantly increasing, reaching the maximum and turning to decreasing sharply towards the conventional 1D Bose gas limit, reproducing the results in previous works [54, 67, 75]. Similarly, a stronger trapping potential plays a more important role and smooths out the hump in the frequency, as shown by the black dashed and dotted lines. Here, we also introduce a critical atom number N_{c3} in Fig. 6(b) where the MF and LHY energies play a competing role against the quantum pressure and the breathing mode frequency reaches the maximum, see also the black dotted lines in Fig. 1. In Fig. 6(c), the mode frequencies are illustrated as a function of trapping strength κ for three values of interaction ratio λ . As the trapping potential gets stronger,

the breathing mode frequency decreases significantly towards the conventional Bose gas limit. Here, a smaller λ leads δg closer to zero, thus the system is more favorable to collapse and ω_b becomes divergent more quickly as κ decreases. In all figures, the dipole mode frequency ω_d equals the harmonic trapping frequency over all the ranges guaranteed by the Kohn theorem, i.e., $\omega_d = \omega_x$, as shown by the numerical calculations (blue lines) and the analytic results (blue crosses). Here, our numerical calculations agree well with the analytic results in Eq. (6) and Eq. (7), denoted by the hollow symbols.

In addition to the above modes governed by the motion of the total density, we further study the spin-dependent collective excitations, i.e., spin dipole and spin breathing modes, by introducing spin-dependent perturbations in Eq. (4) and analyzing the related time-dependent observables. By perturbing the system with a small spin-dependent displacement $\sigma_z \delta x$, the spin dipole mode is excited that can be studied through the time evolution of the associated spin center-of-mass displacement $\langle \sigma_z x(t) \rangle$ as shown in Fig. 7(a). The inset shows its Fourier analysis $\tilde{f}(\omega)$ with some peaks indicating the existence of multiple modes in the related dynamics. Here, the highest peak corresponds to the spin dipole mode at $\omega_{sd} = 4.39\omega_x$, corresponding to an oscillation period of $T_{sd} = 2\pi/\omega_{sd} \approx 1.43/\omega_x$. This can be further verified by the spatiotemporal evolution of the spin density distribution $\delta n(x, t) = n_{\uparrow}(x, t) - n_{\downarrow}(x, t)$ in Fig. 7(b). The relative motion between the two spin components leads to alternating high and low density differences at opposite ends of the cloud, and the higher-frequency modes give rise to small revisions in spin density. As a result, the spin density distribution exhibits a character-

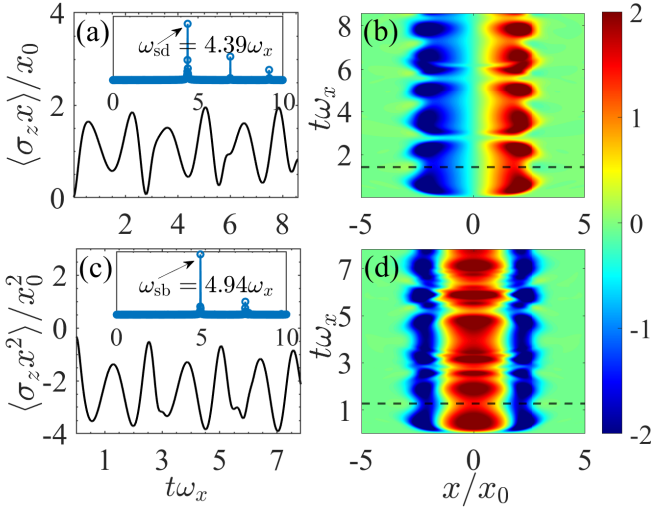


FIG. 7: Illustration of typical time-dependent observables $\langle \sigma_z x \rangle$, $\langle \sigma_z x^2 \rangle$, and contour plots of the spin density distribution $\delta n(x, t) = n_1 - n_2$ for (a, b) spin dipole mode and (c, d) spin breathing mode. The Fourier analyses of the observables are shown in insets, while the dominant peaks at $\omega_{\text{sd}} = 4.39\omega_x$ and $\omega_{\text{sb}} = 4.94\omega_x$ extract the spin breathing and spin breathing mode frequencies, respectively. The corresponding time durations of one period, i.e., $2\pi/\omega_{\text{sd}} \approx 1.43/\omega_x$ and $2\pi/\omega_{\text{sb}} \approx 1.27/\omega_x$, are denoted by the black dashed lines in (b, d).

istic antisymmetric profile that oscillates periodically in time whose period agrees well with T_{sd} shown in a black dashed line. Similarly, we excite the spin breathing mode by introducing a spin-dependent variation of the trapping frequency and show the evolution of the related spin squared radius $\langle \sigma_z x^2 \rangle$ in Fig. 7(c). The inset reveals the spin breathing mode takes a frequency of $\omega_{\text{sb}} = 4.94\omega_x$. This period $T_{\text{sb}} = 2\pi/\omega_{\text{sb}} \approx 1.27/\omega_x$ is further confirmed in the spatiotemporal spin density as shown by the black dashed line in Fig. 7(d). The density of different spin components exhibits distinct alternating behaviors at the center and the tails, i.e., relative trends of expansion and contraction, with the difference in their relative motion reaching a maximum at the half-cycle and returning to a minimum at the full cycle. As a result, the middle and both end regions of the spin density distribution display structures with opposite signs that are symmetric about the origin $x = 0$.

Based on the procedure described in the last paragraph and Fig. 7, the frequencies of spin dipole mode (i.e., blue lines with filled circles) and spin breathing mode (i.e., red lines with filled circles) are extracted and depicted in Fig. 8, as functions of the interaction ratio λ and total atom number N at two values of trapping potential strengths $\kappa = 0.01$ and $\kappa = 0.1$. In Fig. 8(a), both spin mode frequencies show a monotonic dependence on λ , i.e., decreasing sharply as λ rises and tending to saturate. This trend of saturation becomes more

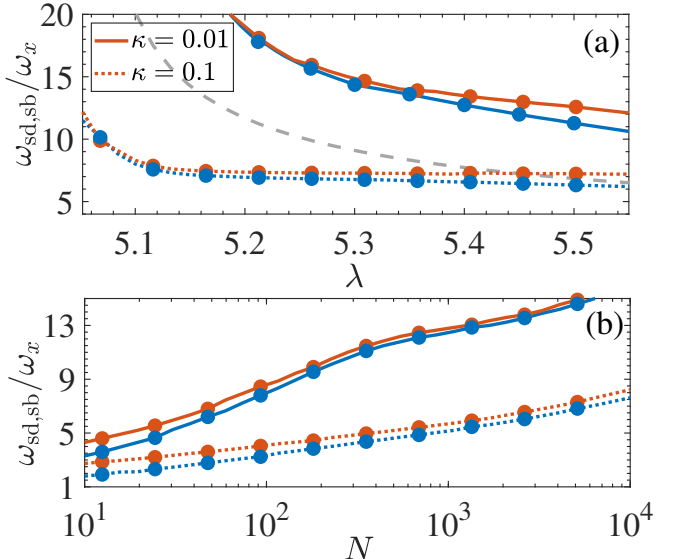


FIG. 8: The spin dipole mode (blue lines with filled circles) and spin breathing mode (red lines with filled circles) frequencies $\omega_{\text{sd},\text{sb}}$ for $\kappa = 0.01$ (solid lines), and $\kappa = 0.1$ (dotted lines), as functions of (a) interaction ratio λ in parameter region II, (b) total atom number N with $\lambda = 5.3$. Other parameters are identical to those in Fig. 6. The gray dashed line indicates the sum-rule prediction of the spin dipole mode frequency $\omega_{\text{sd}}^{\text{analytic}} = \sqrt{\frac{g-g_{12}}{g+g_{12}}}\omega_x$ in the conventional weakly interacting two-component Bose gas.

pronounced for larger κ . This is because the relatively strong trapping potential will compress the droplet to maintain a Gaussian-like wave function or a Thomas-Fermi density distribution, see also the radius in Fig. 4(a) and the breathing mode frequency in Fig. 6(a). Thus, the spin dipole mode frequency tends to approach the sum-rule prediction $\omega_{\text{sd}}^{\text{analytic}} = \sqrt{\frac{g-g_{12}}{g+g_{12}}}\omega_x$ of the conventional weakly interacting symmetric two-component Bose gas [68]. In Fig. 8(b), the frequencies of both spin modes increase monotonically with N , in contrast to the non-monotonic behavior of the breathing mode in Fig. 6(b). A stronger confinement will gradually slow down the upward trend in the frequencies of spin modes.

IV. CONCLUSIONS AND OUTLOOKS

In this work, we have systematically investigated the ground-state properties and collective excitations of one-dimensional quantum droplets in weakly interacting Bose-Bose mixtures with asymmetric intraspin interactions. By numerically solving the extended Gross-Pitaevskii equation and employing complementary theoretical methods—namely, a variational approximation and a sum-rule approach—we have provided a detailed analysis of both static and dynamic behaviors across a

wide range of parameters.

Our results reveal that the asymmetry in intraspin interactions, quantified by the ratio $\lambda = g_1/g_2$, plays a crucial role in shaping the density profiles, root-mean-square radii, peak densities, and excitation spectra of quantum droplets. Similar to the effect of the atom number in previous works, we probe a clear transition from Gaussian-like to flat-top density distributions modulated by increasing λ , a signature of the quantum droplet phase. This transition is further modulated by the strength of the external confinement κ and the total atom number N . We find that, for a fixed trapping strength κ , the radii of both components are identical and increase monotonically with the interaction ratio λ , while their peak densities differ and decrease monotonically with this ratio. Besides, the identical radii of both components in free space exhibit a non-monotonic behavior with the atom number N while their peak densities increase monotonically and turn to saturate at a constant value. We further introduce three critical points N_{c1} , N_{c2} , and N_{c3} to distinguish different regimes and phases in the phase diagrams of the system.

Furthermore, we have studied four typical low-energy collective excitation modes in this system, i.e., the well-studied dipole and breathing modes, and the less-studied spin dipole and spin breathing modes. In our numerical calculations, specific perturbations are designed to excite certain modes, and the corresponding frequencies are extracted from the Fourier analysis of the associated time-dependent observables. The frequencies for the dipole and breathing modes are further verified by the sum-rule analysis based on a super-Gaussian variational ansatz. We find that the dipole mode conforms to Kohn's theorem, oscillating at the trap frequency regardless of interaction asymmetry. In contrast, the breathing mode frequency exhibits a pronounced non-monotonic dependence on N as well as λ , reflecting the competition between mean-field, Lee-Huang-Yang, and quantum pressure contributions. The spin-dependent modes, excited via spin-dependent perturbations, reveal rich dynamics in the relative motion of the two components. Both spin dipole and spin breathing mode frequencies exhibit monotonic dependence on the intra-species interaction asymmetry ratio and total atom number, and the frequencies tend to approach analytic predictions in the relatively stronger confinement limit.

In summary, this work provides a robust theoretical framework for understanding and characterizing asymmetrically interacting quantum droplets, paving the way for further experimental and theoretical advances in the study of beyond-mean-field quantum phenomena. The excellent agreement between numerical extended GPE results and those from the variational and sum-rule approaches underscores the reliability of our methods and the physical insight they provide.

Further questions, such as extension to higher dimensions, the finite-temperature effect, systems with external effects like spin-orbit coupling, and other physical

properties such as phase coherence and superfluidity, remain to be investigated to better understand the exotic self-bound quantum droplet phase. Moreover, the role of beyond-LHY corrections and the dynamics of droplet formation and stability under time-dependent interactions represent promising avenues for future research.

ACKNOWLEDGMENTS

We acknowledge fruitful discussions with Zengqiang Yu and Jia Wang. This work is supported by the Natural Science Foundation of China (Grants No. 12474492, No. 12461160324, No. 12204413 and No. 12247101), the Science Challenge Project (Grant No. TZ2025017), the Science Foundation of Zhejiang Sci-Tech University (Grant No. 21062339-Y), the Fundamental Research Funds for the Central Universities (Grant No. lzujbky-2025-jdzx07), the Natural Science Foundation of Gansu Province (No. 25JRRA799), and the '111 Center' under Grant No. B20063.

Appendix A: more details of the variational approach

In this section, we present more details of the variational approach employed in the main text. The behaviors of the associated variables, as well as the spin atom number ratio, are shown as functions of the interaction ratio.

In our variational approach, we adopt the super-Gaussian variational *Ansatz* in Eq. (5) for the condensate and substitute it into the energy functional. By minimizing the energy with respect to the variables, i.e., $\frac{\partial \epsilon_{tot}}{\partial \alpha}$ and $\frac{\partial \epsilon_{tot}}{\partial \sigma}$, we obtain the coupled equations for the extremum points (α_0, σ_0) as

$$\begin{aligned} & -\frac{\hbar^2 \alpha_0^2 \Gamma(2 - \frac{1}{2\alpha_0})}{m \sigma_0^3 \Gamma(\frac{1}{2\alpha_0})} + \frac{m \omega_x^2 \sigma_0 \Gamma(\frac{3}{2\alpha_0})}{\Gamma(\frac{1}{2\alpha_0})} \\ & -\left(\frac{1}{2}\right)^{\frac{1}{2\alpha_0}} \frac{N \alpha_0 \sqrt{\gamma} (g_{12} + g_2 \sqrt{\gamma})}{\Gamma(\frac{1}{2\alpha_0}) \sigma_0^2 (1 + \sqrt{\gamma})^2} \\ & + \frac{1}{3} \left(\frac{2}{3}\right)^{\frac{1}{2\alpha_0}} \frac{\sqrt{m}}{\pi \hbar} \sqrt{\frac{N \alpha_{1,0}}{\Gamma(\frac{1}{2\alpha_0}) \sigma_0^3}} (g_2 \sqrt{\gamma})^{\frac{3}{2}} = 0, \quad (A1a) \end{aligned}$$

$$\begin{aligned} & \frac{\hbar^2 \Gamma(2 - \frac{1}{2\alpha_0})}{4m \sigma_0^2 \Gamma(\frac{1}{2\alpha_0})} \left[4\alpha_0 + \psi^{(0)}(2 - \frac{1}{2\alpha_0}) + \psi^{(0)}(\frac{1}{2\alpha_0}) \right] \\ & + \frac{m \omega_x^2 \sigma_0^2 \Gamma(\frac{-3}{2\alpha_0})}{4\alpha_0^2 \Gamma(\frac{1}{2\alpha_0})} \left[\psi^{(0)}(\frac{1}{2\alpha_0}) - 3\psi^{(0)}(\frac{3}{2\alpha_0}) \right] \\ & + \left(\frac{1}{2}\right)^{\frac{1}{2\alpha_0}} \frac{N \sqrt{\gamma} (g_{12} + g_2 \sqrt{\gamma}) \ln 2 + 2\alpha_0 + \psi^{(0)}(\frac{1}{2\alpha_0})}{\sigma_0 (\sqrt{\gamma} + 1)^2} \frac{2\alpha_0 \Gamma(\frac{1}{2\alpha_0})}{2\alpha_0 \Gamma(\frac{1}{2\alpha_0})} \\ & - \frac{2}{3} \left(\frac{2}{3}\right)^{\frac{1}{2\alpha_0}} \sqrt{\frac{N m \alpha_0}{\sigma_0 \Gamma(\frac{1}{2\alpha_0})}} \frac{2\alpha_0 - 2 \ln \frac{2}{3} + \psi^{(0)}(\frac{1}{2\alpha_0})}{4\alpha_0^2 \pi \hbar} (g_2 \sqrt{\gamma})^{\frac{3}{2}} = 0, \quad (A1b) \end{aligned}$$

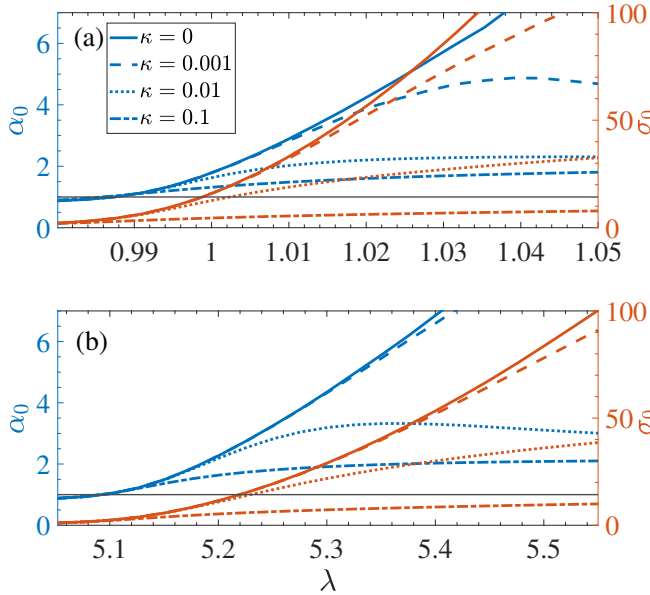


FIG. 9: The extreme points (α_0, σ_0) in Eq. (5) at the ground states, as functions of the interaction strength ratio λ at different values of trapping potential strength $\kappa = 0$ (solid lines), 0.001 (dashed lines), 0.01 (dotted lines), and 0.1 (dash-dotted lines).

with the 0-th order Polygamma function $\psi^{(0)}(x) \equiv \frac{\Gamma'(x)}{\Gamma(x)}$ denoting the differentiation of the Gamma Function $\Gamma(x)$. Therefore, after numerically calculating the extremum points (α_0, σ_0) from the above coupled equations, we can reconstruct the wave function of the condensate by substituting them back into Eq. (5). In Fig. 9, the variational width σ_0 and the exponent factor α_0 in the variational ansatz are presented as functions of the interaction ratio λ . The horizontal gray solid line indicates the standard Gaussian function corresponding to $\alpha_0 = 1$. It is clearly seen that the super-Gaussian parameter α_0 of the quantum droplet in blue curves increases significantly from around 1 with λ , reflecting a gradual transition of the density profile from Gaussian-like to flat-top structure. At relatively large interaction ratios and at different trapping potential strengths, we can clearly see that the exponent factors α_0 in blue curves stay far away from 1. Particularly, the exponent factor becomes relatively large in the flat-top droplet regime, where a Gaussian state fails to capture the structural

features of flat-top states. This reveals the rationality of the use of the adopted super-Gaussian ansatz with a variable exponent factor here across different parameter regimes instead of a conventional Gaussian function for the condensate wave function.

In addition, Petrov predicted that, near the mean-field collapsing point, the density ratio of two spin components in quantum droplets is fixed and associated with the intraspin scattering lengths as $n_2/n_1 = \sqrt{a_{11}/a_{22}}$ [3], i.e., $n_2/n_1 = \sqrt{\lambda}$. By employing a bosonic pairing theory, Hu *et. al* showed that this density ratio can vary over

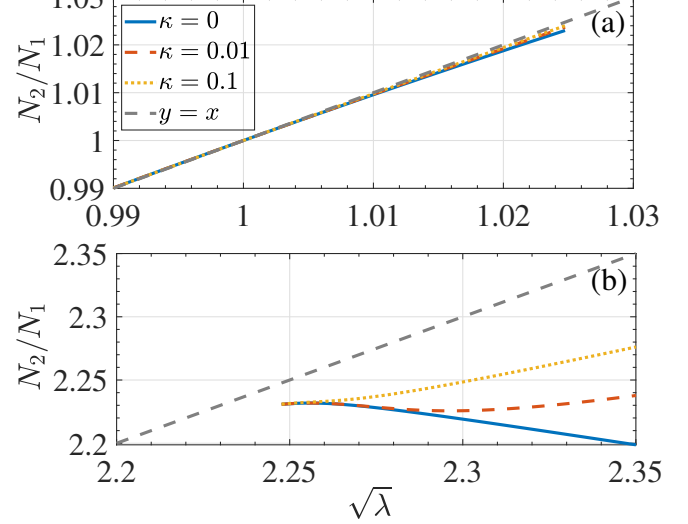


FIG. 10: The ratio of two spin atom numbers or atom number imbalance N_2/N_1 as a function of the square root of the interaction ratio $\sqrt{\lambda}$ at different values of trapping potential strength $\kappa = 0$ (solid lines), 0.01 (dashed lines), and 0.1 (dotted lines) while the dash-dotted line indicates the linear line $y = x$.

a sizeable range that could be far away from the fixed ratio $\sqrt{\lambda}$ [76]. In Fig. 10, by numerically solving the extended GPE in Eq. (3), the atom number ratio N_2/N_1 is shown as a function of $\sqrt{\lambda}$. In general, the numerical results show that this ratio is not fixed with the variable $\sqrt{\lambda}$ except for the regime when $\sqrt{\lambda}$ is very close to 1. However, the fixed ratio $n_2/n_1 = \sqrt{\lambda}$ is adopted in our variational approach and the related calculations, such as density profiles, droplet width, peak density, collective excitation frequency, show no significant difference with the numerical results.

[1] T. D. Lee, K. Huang, and C. N. Yang, Eigenvalues and eigenfunctions of a bose system of hard spheres and its low-temperature properties, *Phys. Rev.* **106**, 1135 (1957).

[2] A. Bulgac, Dilute quantum droplets, *Phys. Rev. Lett.* **89**, 050402 (2002).

[3] D. S. Petrov, Quantum mechanical stabilization of a colapsing bose-bose mixture, *Phys. Rev. Lett.* **115**, 155302 (2015).

[4] D. S. Petrov and G. E. Astrakharchik, Ultradilute low-dimensional liquids, *Phys. Rev. Lett.* **117**, 100401 (2016).

[5] D. S. Petrov, Beyond-mean-field effects in mixtures: few-body and many-body aspects, arXiv preprint

arXiv:2312.05336 [10.48550/arXiv.2312.05336](https://arxiv.org/abs/2312.05336) (2023).

- [6] C. R. Cabrera, L. Tanzi, J. Sanz, B. Naylor, P. Thomas, P. Cheiney, and L. Tarruell, Quantum liquid droplets in a mixture of bose-einstein condensates, *Science* **359**, 301 (2018).
- [7] G. Semeghini, G. Ferioli, L. Masi, C. Mazzinghi, L. Wolswijk, F. Minardi, M. Modugno, G. Modugno, M. Inguscio, and M. Fattori, Self-bound quantum droplets of atomic mixtures in free space, *Phys. Rev. Lett.* **120**, 235301 (2018).
- [8] P. Cheiney, C. R. Cabrera, J. Sanz, B. Naylor, L. Tanzi, and L. Tarruell, Bright soliton to quantum droplet transition in a mixture of bose-einstein condensates, *Phys. Rev. Lett.* **120**, 135301 (2018).
- [9] C. D'Errico, A. Burchianti, M. Prevedelli, L. Salasnich, F. Ancilotto, M. Modugno, F. Minardi, and C. Fort, Observation of quantum droplets in a heteronuclear bosonic mixture, *Phys. Rev. Res.* **1**, 033155 (2019).
- [10] G. Ferioli, G. Semeghini, L. Masi, G. Giusti, G. Modugno, M. Inguscio, A. Gallemí, A. Recati, and M. Fattori, Collisions of self-bound quantum droplets, *Phys. Rev. Lett.* **122**, 090401 (2019).
- [11] T. G. Skov, M. G. Skou, N. B. Jørgensen, and J. J. Arlt, Observation of a lee-huang-yang fluid, *Phys. Rev. Lett.* **126**, 230404 (2021).
- [12] Z. Guo, F. Jia, L. Li, Y. Ma, J. M. Hutson, X. Cui, and D. Wang, Lee-huang-yang effects in the ultracold mixture of ^{23}Na and ^{87}Rb with attractive interspecies interactions, *Phys. Rev. Res.* **3**, 033247 (2021).
- [13] L. Cavicchioli, C. Fort, F. Ancilotto, M. Modugno, F. Minardi, and A. Burchianti, Dynamical formation of multiple quantum droplets in a bose-bose mixture, *Phys. Rev. Lett.* **134**, 093401 (2025).
- [14] H. Kadau, M. Schmitt, M. Wenzel, C. Wink, T. Maier, I. Ferrier-Barbut, and T. Pfau, Observing the rosenweig instability of a quantum ferrofluid, *Nature* **530**, 194 (2016).
- [15] I. Ferrier-Barbut, H. Kadau, M. Schmitt, M. Wenzel, and T. Pfau, Observation of quantum droplets in a strongly dipolar bose gas, *Phys. Rev. Lett.* **116**, 215301 (2016).
- [16] L. Chomaz, S. Baier, D. Petter, M. Mark, F. Wächtler, L. Santos, and F. Ferlaino, Quantum-fluctuation-driven crossover from a dilute bose-einstein condensate to a macrodroplet in a dipolar quantum fluid, *Phys. Rev. X* **6**, 041039 (2016).
- [17] M. Schmitt, M. Wenzel, F. Böttcher, I. Ferrier-Barbut, and T. Pfau, Self-bound droplets of a dilute magnetic quantum liquid, *Nature* **539**, 259 (2016).
- [18] L. Tanzi, E. Lucioni, F. Famà, J. Catani, A. Fioretti, C. Gabbanini, R. N. Bisset, L. Santos, and G. Modugno, Observation of a dipolar quantum gas with metastable supersolid properties, *Phys. Rev. Lett.* **122**, 130405 (2019).
- [19] F. Böttcher, M. Wenzel, J.-N. Schmidt, M. Guo, T. Langen, I. Ferrier-Barbut, T. Pfau, R. Bombín, J. Sánchez-Baena, J. Boronat, *et al.*, Dilute dipolar quantum droplets beyond the extended gross-pitaevskii equation, *Phys. Rev. Res.* **1**, 033088 (2019).
- [20] D. Rakshit, T. Karpiuk, M. Brewczyk, and M. Gajda, Quantum Bose-Fermi droplets, *SciPost Phys.* **6**, 079 (2019).
- [21] D. Rakshit, T. Karpiuk, P. Zin, M. Brewczyk, M. Lewenstein, and M. Gajda, Self-bound bose-fermi liquids in lower dimensions, *New Journal of Physics* **21**, 073027 (2019).
- [22] J. C. Smith, D. Baillie, and P. B. Blakie, Quantum droplet states of a binary magnetic gas, *Phys. Rev. Lett.* **126**, 025302 (2021).
- [23] R. N. Bisset, L. A. P. n. Ardila, and L. Santos, Quantum droplets of dipolar mixtures, *Phys. Rev. Lett.* **126**, 025301 (2021).
- [24] Y. V. Kartashov, G. E. Astrakharchik, B. A. Malomed, and L. Torner, Frontiers in multidimensional self-trapping of nonlinear fields and matter, *Nat. Rev. Phys.* **1**, 185 (2019).
- [25] F. Böttcher, J.-N. Schmidt, J. Hertkorn, K. S. Ng, S. D. Graham, M. Guo, T. Langen, and T. Pfau, New states of matter with fine-tuned interactions: quantum droplets and dipolar supersolids, *Rep. Prog. Phys.* **84**, 012403 (2021).
- [26] Z.-H. Luo, W. Pang, B. Liu, Y.-Y. Li, and B. A. Malomed, A new form of liquid matter: Quantum droplets, *Frontiers of Physics* **16**, 32201 (2021).
- [27] M. Guo and T. Pfau, A new state of matter of quantum droplets, *Frontiers of Physics* **16**, 32202 (2021).
- [28] V. Cikojević, K. Dželalija, P. Stipanović, L. Vranješ Markić, and J. Boronat, Ultradilute quantum liquid drops, *Phys. Rev. B* **97**, 140502 (2018).
- [29] L. Parisi, G. Astrakharchik, and S. Giorgini, Liquid state of one-dimensional bose mixtures: a quantum monte carlo study, *Phys. Rev. Lett.* **122**, 105302 (2019).
- [30] C. Staudinger, F. Mazzanti, and R. E. Zillich, Self-bound bose mixtures, *Phys. Rev. A* **98**, 023633 (2018).
- [31] H. Hu and X.-J. Liu, Consistent theory of self-bound quantum droplets with bosonic pairing, *Phys. Rev. Lett.* **125**, 195302 (2020).
- [32] Q. Gu and L. Yin, Phonon stability and sound velocity of quantum droplets in a boson mixture, *Phys. Rev. B* **102**, 220503 (2020).
- [33] J. Pan, S. Yi, and T. Shi, Quantum phases of self-bound droplets of bose-bose mixtures, *Phys. Rev. Res.* **4**, 043018 (2022).
- [34] L. He, H. Li, W. Yi, and Z.-Q. Yu, Quantum criticality of liquid-gas transition in a binary bose mixture, *Phys. Rev. Lett.* **130**, 193001 (2023).
- [35] A. Cappellaro, T. Macrì, and L. Salasnich, Collective modes across the soliton-droplet crossover in binary bose mixtures, *Phys. Rev. A* **97**, 053623 (2018).
- [36] G. Spada, S. Pilati, and S. Giorgini, Attractive solution of binary bose mixtures: Liquid-vapor coexistence and critical point, *Phys. Rev. Lett.* **131**, 173404 (2023).
- [37] Y. V. Kartashov, B. A. Malomed, L. Tarruell, and L. Torner, Three-dimensional droplets of swirling superfluids, *Phys. Rev. A* **98**, 013612 (2018).
- [38] Y. Li, Z. Chen, Z. Luo, C. Huang, H. Tan, W. Pang, and B. A. Malomed, Two-dimensional vortex quantum droplets, *Phys. Rev. A* **98**, 063602 (2018).
- [39] Y. V. Kartashov, B. A. Malomed, and L. Torner, Metastability of quantum droplet clusters, *Phys. Rev. Lett.* **122**, 193902 (2019).
- [40] S. R. Otajonov, E. N. Tsoy, and F. K. Abdullaev, Variational approximation for two-dimensional quantum droplets, *Phys. Rev. E* **102**, 062217 (2020).
- [41] N. Guebli and A. Boudjemâa, Quantum self-bound droplets in bose-bose mixtures: Effects of higher-order quantum and thermal fluctuations, *Phys. Rev. A* **104**, 023310 (2021).
- [42] P. Zin, M. Pylak, T. Wasak, M. Gajda, and Z. Idziaszek,

Quantum bose-bose droplets at a dimensional crossover, *Phys. Rev. A* **98**, 051603 (2018).

[43] V. Cikojević, L. V. c. v. Markić, M. Pi, M. Barranco, F. Ancilotto, and J. Boronat, Dynamics of equilibration and collisions in ultradilute quantum droplets, *Phys. Rev. Res.* **3**, 043139 (2021).

[44] T. Mithun, S. Mistakidis, P. Schmelcher, and P. Kevrekidis, Statistical mechanics of one-dimensional quantum droplets, *Phys. Rev. A* **104**, 033316 (2021).

[45] Y. Hu, Y. Fei, X. Chen, and Y. Zhang, Collisional dynamics of symmetric two-dimensional quantum droplets, *Front. Phys.* **17**, 61505 (2022).

[46] M. N. Tengstrand and S. Reimann, Droplet-superfluid compounds in binary bosonic mixtures, *Phys. Rev. A* **105**, 033319 (2022).

[47] S. Nikolaou, G. Kavoulakis, and M. Ögren, Rotating quantum droplets confined in a harmonic potential, *Phys. Rev. A* **108**, 053309 (2023).

[48] G. E. Astrakharchik and B. A. Malomed, Dynamics of one-dimensional quantum droplets, *Phys. Rev. A* **98**, 013631 (2018).

[49] S. R. Otajonov, E. N. Tsoy, and F. K. Abdullaev, Stationary and dynamical properties of one-dimensional quantum droplets, *Phys. Rev. A* **383**, 125980 (2019).

[50] M. Tylutki, G. E. Astrakharchik, B. A. Malomed, and D. S. Petrov, Collective excitations of a one-dimensional quantum droplet, *Phys. Rev. A* **101**, 051601 (2020).

[51] H. Hu and X.-J. Liu, Collective excitations of a spherical ultradilute quantum droplet, *Phys. Rev. A* **102**, 053303 (2020).

[52] P. Stürmer, M. N. Tengstrand, R. Sachdeva, and S. M. Reimann, Breathing mode in two-dimensional binary self-bound bose-gas droplets, *Phys. Rev. A* **103**, 053302 (2021).

[53] L. Dong, K. Shi, and C. Huang, Internal modes of two-dimensional quantum droplets, *Phys. Rev. A* **106**, 053303 (2022).

[54] X. Du, Y. Fei, X.-L. Chen, and Y. Zhang, Ground-state properties and bogoliubov modes of a harmonically trapped one-dimensional quantum droplet, *Phys. Rev. A* **108**, 033312 (2023).

[55] Y. Fei, X. Du, X.-L. Chen, and Y. Zhang, Collective excitations in two-dimensional harmonically trapped quantum droplets, *Phys. Rev. A* **109**, 053309 (2024).

[56] T. A. Flynn, L. Parisi, T. P. Billam, and N. G. Parker, Quantum droplets in imbalanced atomic mixtures, *Phys. Rev. Res.* **5**, 033167 (2023).

[57] T. A. Flynn, N. A. Keepfer, N. G. Parker, and T. P. Billam, Harmonically trapped imbalanced quantum droplets, *Phys. Rev. Res.* **6**, 013209 (2024).

[58] Y. V. Kartashov and D. A. Zezyulin, Multipole quantum droplets in quasi-one-dimensional asymmetric mixtures, *Phys. Rev. A* **110**, L021304 (2024).

[59] A. Sartori, J. Marino, S. Stringari, and A. Recati, Spin-dipole oscillation and relaxation of coherently coupled bose-einstein condensates, *New Journal of Physics* **17**, 093036 (2015).

[60] T. Bienaimé, E. Fava, G. Colzi, C. Mordini, S. Serafini, C. Qu, S. Stringari, G. Lamporesi, and G. Ferrari, Spin-dipole oscillation and polarizability of a binary bose-einstein condensate near the miscible-immiscible phase transition, *Phys. Rev. A* **94**, 063652 (2016).

[61] E. Fava, T. Bienaimé, C. Mordini, G. Colzi, C. Qu, S. Stringari, G. Lamporesi, and G. Ferrari, Observation of spin superfluidity in a bose gas mixture, *Phys. Rev. Lett.* **120**, 170401 (2018).

[62] T. Mithun, A. Maluckov, K. Kasamatsu, B. A. Malomed, and A. Khare, Modulational instability, inter-component asymmetry, and formation of quantum droplets in one-dimensional binary bose gases, *Symmetry* **12**, 174 (2020).

[63] Y. Li, G. I. Martone, and S. Stringari, Sum rules, dipole oscillation and spin polarizability of a spin-orbit coupled quantum gas, *Europhysics Letters* **99**, 56008 (2012).

[64] Note that we have tried the variational *Ansatz* with four variables, i.e., two widths $\sigma_{1,2}$, and exponent factors $\alpha_{1,2}$. And after the minimization, they are equal ($\sigma_1 = \sigma_2$ and $\alpha_1 = \alpha_2$) for each spin.

[65] S. Stringari, Collective excitations of a trapped bose-condensed gas, *Phys. Rev. Lett.* **77**, 2360 (1996).

[66] F. Dalfovo, S. Giorgini, L. P. Pitaevskii, and S. Stringari, Theory of bose-einstein condensation in trapped gases, *Rev. Mod. Phys.* **71**, 463 (1999).

[67] C. Menotti and S. Stringari, Collective oscillations of a one-dimensional trapped bose-einstein gas, *Phys. Rev. A* **66**, 043610 (2002).

[68] L. Pitaevskii and S. Stringari, *Bose-Einstein condensation and superfluidity*, Vol. 164 (Oxford University Press, 2016).

[69] A. Görlitz, J. M. Vogels, A. E. Leanhardt, C. Raman, T. L. Gustavson, J. R. Abo-Shaeer, A. P. Chikkatur, S. Gupta, S. Inouye, T. Rosenband, and W. Ketterle, Realization of bose-einstein condensates in lower dimensions, *Phys. Rev. Lett.* **87**, 130402 (2001).

[70] F. Schreck, L. Khaykovich, K. L. Corwin, G. Ferrari, T. Bourdel, J. Cubizolles, and C. Salomon, Quasipure bose-einstein condensate immersed in a fermi sea, *Phys. Rev. Lett.* **87**, 080403 (2001).

[71] M. Greiner, I. Bloch, O. Mandel, T. W. Hänsch, and T. Esslinger, Exploring phase coherence in a 2d lattice of bose-einstein condensates, *Phys. Rev. Lett.* **87**, 160405 (2001).

[72] M. Olshanii, Atomic scattering in the presence of an external confinement and a gas of impenetrable bosons, *Phys. Rev. Lett.* **81**, 938 (1998).

[73] C. D'Errico, M. Zaccanti, M. Fattori, G. Roati, M. Inguscio, G. Modugno, and A. Simoni, Feshbach resonances in ultracold 39k, *New Journal of Physics* **9**, 223 (2007).

[74] L. Parisi and S. Giorgini, Quantum droplets in one-dimensional bose mixtures: A quantum monte carlo study, *Phys. Rev. A* **102**, 023318 (2020).

[75] T. Kimura, Breathing modes of bose-einstein condensates in highly asymmetric traps, *Phys. Rev. A* **66**, 013608 (2002).

[76] H. Hu, J. Wang, H. Pu, and X.-J. Liu, Breakdown of the single-mode description of ultradilute quantum droplets in binary bose mixtures: A perspective from a microscopic bosonic pairing theory, *Phys. Rev. A* **111**, 023309 (2025).